


Rapidly Enhanced Spin-Polarization Injection in an Optically Pumped Spin Ratchet

Adrishia Sarkar,^{1,†} Brian Blankenship^{1,†}, Emanuel Druga¹, Arjun Pillai,¹ Ruhee Nirodi,¹ Siddharth Singh¹, Alexander Oddo,¹ Paul Reshetikhin,¹ and Ashok Ajoy^{1,2,*}

¹Department of Chemistry, University of California, Berkeley, Berkeley, California 94720, USA

²Chemical Sciences Division, Lawrence Berkeley National Laboratory, Berkeley, California 94720, USA

 (Received 28 January 2022; revised 13 April 2022; accepted 9 August 2022; published 28 September 2022)

Rapid injection of spin polarization into an ensemble of nuclear spins is a problem of broad interest, spanning dynamic nuclear polarization (DNP) to quantum information science. We report on a strategy to boost the spin-injection rate by exploiting electrons that can be rapidly polarized via high-power optical pumping. We demonstrate this in a model system of nitrogen-vacancy center electrons injecting polarization into a bath of ¹³C nuclei in diamond. We deliver > 20 W of continuous, nearly isotropic, optical power to the sample, constituting a substantially higher power than in previous experiments. Through a spin-ratchet polarization transfer mechanism, we show boosts in spin-injection rates by over 2 orders of magnitude. Our experiments elucidate bottlenecks in the DNP process caused by rates of electron polarization, polarization transfer to proximal nuclei, and spin diffusion. This work demonstrates opportunities for rapid spin injection employing nonthermally generated electron polarization, and has relevance to a broad class of experimental systems, including in DNP, quantum sensing, and spin-based MASERs (microwave amplification by stimulated emission of radiation).

DOI: [10.1103/PhysRevApplied.18.034079](https://doi.org/10.1103/PhysRevApplied.18.034079)

I. INTRODUCTION

The injection of polarization into an ensemble of nuclear spins is a task of central importance in a variety of contexts. Not only is it the basis for dynamic nuclear polarization (DNP) [1,2], it is also important for the initialization of spin-based quantum information processors [3–6], quantum sensors [7–9], and in emerging applications in spintronics [10–12]. Critical to such applications is the *rate* at which polarization can be injected, measured, for instance, in terms of total angular momenta injected per unit time. For DNP applications, this rate ultimately determines the possible throughput of hyperpolarized spectroscopy and imaging [13].

In this paper we demonstrate enhanced rates of spin injection employing *nonthermally* generated electron polarization [10,14,15]. We focus on a model DNP system of optically polarizable nitrogen-vacancy (N-V) center electrons (*e*) in diamond and consider polarization transfer to lattice ¹³C nuclei (*n*) [16,17]. Considering Fig. 1(a), the buildup of bulk nuclear polarization proceeds through a relayed process, and the overall rate of bulk spin injection is determined as an interplay between the rates at which (i) electron polarization is generated, κ_e , (ii) polarization

is transferred from electrons to proximal nuclei, κ_r , and (iii) polarization is relayed to distant (bulk) nuclei via spin diffusion, κ_d [18]. In thermal DNP settings, $\kappa_e \approx T_{1e}^{-1}$ is system specific, cannot be controlled, and is relatively slow at low temperatures [19–21]; likewise, κ_r is constrained by the available microwave (MW) power at high magnetic fields [22–24]. In contrast, in optical DNP, κ_e is determined by laser intensity, potentially allowing access to the $\kappa_e \gg T_{1e}^{-1}$ regime wherein source polarization can be rapidly generated. Simultaneously, optical *e* polarization can be carried out at low fields where high MW powers are readily accessible. In turn, this enables rapidly transmitting *e* polarization to nuclei via high-power MWs, significantly enhancing the rate of hyperpolarization.

A key contribution of this paper is the ability to deliver high optical power continuously to the electrons, allowing us to approach the $\kappa_e > T_{1e}^{-1}$ regime (Appendix A). Time-averaged optical power here (> 20 W) is substantially higher than previous experiments (Appendix B). We then demonstrate an approach to increase the polarization injection rate through a “lockstep” increase in laser and MW power at low fields. We identify hyperpolarization *rate limits* by delineating experimental regimes where each of the three rates in Fig. 1(a) individually bottleneck polarization injection. Ultimately, we show how high-power optical DNP can yield significant gains in the polarization rate, boosted by as much as 2 orders

*ashokaj@berkeley.edu

†Equal contribution

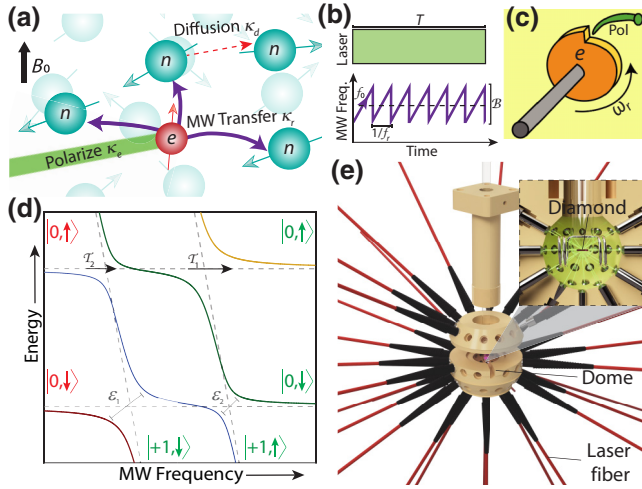


FIG. 1. Spin ratchet ^{13}C hyperpolarization. (a) *Schematic lattice* consisting of an electron e (red) and nuclei n (blue). Hyperpolarization occurs through optical polarization of the electron (N- V center), polarization transfer to directly coupled nuclei (^{13}C), and spin diffusion to bulk nuclei. Corresponding rate coefficients $\{\kappa_e, \kappa_r, \kappa_d\}$ are depicted. (b) *DNP protocol* comprises a continuous-wave (cw) laser and swept MWs applied for period T . MW sweeps, at rate $f_r = \omega_r/2\pi$, are applied over bandwidth \mathcal{B} . (c) *Spin ratchet*. MW sweeps at rate ω_r drive optically generated e polarization to nuclei akin to cranks of a ratchet. (d) *DNP mechanism*. Polarization transfer occurs via MW-driven traversals of cascaded Landau-Zener anticrossings. Shown is the case for a single e - n system (N- V - ^{13}C). Energy gaps $\varepsilon_{1,2}$ are conditioned on the nuclear state (see Appendix C). (e) *Experimental setup*. Thirty approximate 0.8-W lasers (mounted on vertical walls) deliver optical excitation to the sample via optical fibers. Sample is positioned at the center, with lasers arranged in a dome-shaped configuration. Inset: enlarged view of the dome center showing the diamond sample and split MW coil employed for hyperpolarization.

of magnitude compared to conventional methods. Rapid hyperpolarization obtained here opens avenues for quantum sensors (e.g., gyroscopes [25,26] and spin sensors [27]) constructed out of hyperpolarized nuclear spins. Our approach is also readily generalizable to other systems, including optically pumped triplet molecular systems [28, 29] and MASERs (microwave amplification by stimulated emission of radiation) [30,31].

System.—In these experiments, we employ a single-crystal diamond sample with about 1 ppm N- V concentration and natural abundance ^{13}C . The inter-N- V spacing is about 24 nm [32,33] and the ^{13}C lattice density is about 0.92 nm^{-3} . The overall polarization memory time for the system [33] is set as $T_{1n} \approx 5$ min. In what follows, we refer to the incident optical and MW power in watts as η_e and η_r , respectively. These are related to $\{\kappa_e, \kappa_r\}$ in Fig. 1(a), but instead denote experimentally controllable parameters.

DNP is excited at $B_0 = 36$ mT through a mechanism involving cw optical and swept MW irradiation [Fig. 1(b)]

for period T [34,35]. Nitrogen-vacancy centers are optically polarized to the $m_s = 0$ state, yielding an e polarization, $P_e(t) = 1 - \exp(-t\kappa_e)$, assuming a monoexponential rate constant κ_e . In reality, $\kappa_e \approx c_e\eta_e$ is approximately proportional to the optical power applied. Precisely quantifying the absolute e polarization is difficult due to dependence on several factors (e.g., interconversion between N- V charge states [36,37]). However, optically generated polarization obviates the need for high magnetic fields for hyperpolarization. Lower fields come with significant advantages, such as the availability of high MW powers at low frequencies.

In our protocol, each MW sweep event injects polarization into e -proximal nuclei, akin to a “ratchet” [Fig. 1(c)]. Bulk polarization is then readout via rf induction at 7 T. We employ pulsed spin-lock readout [38,39] that permits interrogation of the ^{13}C precession for multiple minute-long periods, with a decay constant $T_2 > 20$ s [40]. Signal is accumulated for the entire period and sampled every 1 ns in windows between the pulses. As a result, we obtain high measurement fidelity, with integrated SNR as high as 10^8 per shot [40]. We employ this high sensitivity to unravel the rate-limiting factors that affect polarization injection rates.

Ratchet-driven polarization.—To elucidate the hyperpolarization mechanism, consider that the MW sweeps have an instantaneous frequency, $f_{\text{MW}}(t) = \mathcal{B}f_r t + f_0 - \mathcal{B}/2$ [Fig. 1(b)], where \mathcal{B} is the sweep bandwidth around f_0 , the electronic spectral center, and f_r is the sweep rate. The rate f_r plays a key role in setting the ultimate rate of bulk hyperpolarization buildup. Every sweep event transfers a finite amount of polarization, and the total number of sweeps, Tf_r , is curtailed by the nuclear T_{1n} . Ideal ratchet operation involves maximizing f_r while maintaining high polarization transfer efficiency *per* sweep. Optimal operation occurs when the sweep rate $f_r = f_{\text{opt}}$, and can be derived by measuring how the polarization buildup rate $\dot{P}(f_r)$ depends on the interplay of rates in Fig. 1(a) (see Appendix C).

Consider that the e - n Hamiltonian for N nuclei [Fig. 1(a)] in the rotating frame at field B_0 has the form [41]

$$\mathcal{H}(\omega_{\text{MW}}) = (\Delta - \gamma_e B_0) S_z^2 + \Omega_e S_z + \Omega_e S_x + \sum_{j=1}^N [\omega_j^{(0)} \mathcal{P}_0 I_{zj} + \omega_j^{(1)} \mathcal{P}_1 I_{zj}], \quad (1)$$

where $\omega_{\text{MW}} = 2\pi f_{\text{MW}}$, S (I) refers to electron (nuclear) operators, and $\gamma_{e,n}$ are the respective magnetogyric ratios. The first two terms in Eq. (1) denote the N- V zero-field splitting ($\Delta = 2.87$ GHz) and Zeeman field; Ω_e is the e -Rabi frequency ($\Omega_e = c_r \eta_r$) proportional to the MW power applied, and we assume an N- V axis aligned with \mathbf{B}_0 (along \hat{z}). The last term in Eq. (1) describes the nuclear field in either electronic manifold— \mathcal{P}_0 and \mathcal{P}_1

are projection operators in the $m_s = 0$ and $m_s = 1$ manifolds, and the nuclear resonance frequencies herein are $\omega_j^{(0)}$ and $\omega_j^{(1)}$, respectively [41]: $\omega_j^{(0)} \approx \omega_n + \gamma_e B_0 A_j^\perp / \Delta$ and $\omega_j^{(1)} = [(\omega_n + A_j^\parallel)^2 + (A_j^\perp)^2]^{1/2}$, where $\omega_n = \gamma_n B_0$ and $A_j = A_j^\parallel \hat{z} + A_j^\perp \hat{x}$ is the hyperfine coupling.

Spin-ratchet polarization transfer is simplest to illustrate for a single e - n system [41,42]. Diagonalization leads to four Landau-Zener level anticrossings (LZ LACs), with energy gaps, $\varepsilon_1 \approx c_r \eta_r$ and $\varepsilon_2 \approx 2c_r \eta_r A_1^\perp / (\omega_n + A_1^\parallel)$ [see Fig. 1(d)], such that $\varepsilon_2 < \varepsilon_1$ (here we set $\hbar = 1$). Swept MWs cause a traversal through this LZ-LAC cascade. Its action can be evaluated under simplifying approximations that capture the experiments [41]: (i) LZ LACs are assumed to be traversed sequentially and (ii) e repolarization is assumed to occur at the start of every sweep event. This entails negligible laser action at the LZ LACs, valid when $\mathcal{B} \gg \varepsilon_{1,2}$, as in our experiments. Hyperpolarization is generated because the energy gaps are conditioned on the nuclear state; traversals through the LZ LACs are differentially adiabatic or diabatic, leading to a population bias towards one nuclear state (here $|\downarrow\rangle$). Population bifurcation at a LZ LAC is set by its adiabaticity and captured by respective tunneling probabilities $\mathcal{T}_{1,2}(f_r) = \exp(-\varepsilon_{1,2}^2 / f_r \mathcal{B})$ [Fig. 1(d)]. Hyperpolarization occurs when sweep rates f_r are such that $\mathcal{T}_1 \rightarrow 0$ (adiabatic) and $\mathcal{T}_2 \neq 0$ (diabatic) [41]. The rate of polarization buildup is then (see Appendix C)

$$\dot{P}(f_r) \approx f_r \left[1 - \exp\left(\frac{-c_e \eta_e}{f_r}\right) \right] [(1 - \mathcal{T}_1)\{1 - (2\mathcal{T}_2 - 1)^2\}]. \quad (2)$$

The first term in square brackets is the rate of e polarization and the second term captures the $e \rightarrow n$ polarization transfer efficiency per sweep. An optimal rate, f_{opt} , occurs when $d\dot{P}/df_r = 0$.

It is intuitive to see why an optimal rate f_{opt} should exist. More rapid sweeps (high f_r) can allow faster ratchet operation, but comes at the cost of (i) reduced electron polarization and (ii) lower transfer efficiency per sweep because the differential adiabaticity in Fig. 1(d) is compromised. At very high f_r , $\mathcal{T}_1 \approx \mathcal{T}_2 \approx 1$ and $\dot{P} \rightarrow 0$. Therefore, f_{opt} reflects an overall rate limit for $e \rightarrow n$ polarization transfer, and defines the rate at which the ratchet [Fig. 1(c)] should be operated. The physics of direct $e \rightarrow n$ polarization transfer is essentially unchanged from Eq. (2) even for large N [41,43]; however, since experiments primarily probe *bulk* nuclei, there is a non-negligible role from spin diffusion.

Importantly, Eq. (2) suggests that the rate of polarization transfer, encoded in f_{opt} , can be enhanced through a simultaneous increase in laser and MW power—higher η_e allows faster e repolarization, and higher η_r permits faster sweeps while maintaining differential adiabaticity. This is the key insight we exploit in this work. In the ultimate limit, the

spin-ratchet hyperpolarization rate (encoded by f_{opt}) is only limited by spin diffusion.

Enhanced optical excitation.—Polarization rates here can exceed that of conventional DNP because electrons can be optically polarized faster than T_{1e}^{-1} , and this polarization can be rapidly transferred to proximal nuclei. We develop a laser delivery apparatus that enables continuous sample irradiation at $\eta_e > 20$ W. The apparatus [Fig. 1(e)] design and construction is detailed in Appendix A. It consists of a three-dimensional (3D) printed dome-shaped structure (“laser dome”) that houses 30 multimode fibers attached to diode lasers (approximately 0.8 W each). To manage sample heating associated with high optical powers, we design an *in situ* heat exchanger. Its performance (detailed in Appendix A) is highly efficient: even at sustained 24 W optical power (an intensity of approximately 0.19 kW/cm²) employing thirty lasers, the steady-state temperature reached in the sample vicinity is less than 30 °C.

II. RESULTS

Lockstep polarization increase.—In the ratchet model without spin diffusion, f_{opt} plays a key role as a proxy for the rate of nuclear spin-polarization injection. We now demonstrate that high-power optical delivery via the apparatus in Fig. 1(e), combined with simultaneous high MW power, can yield significant enhancements to f_{opt} , and thereby spin-injection rates. In parallel, we quantify the rate limits for bulk polarization buildup as an interplay of the rates discussed in Fig. 1(a).

Consider first the data presented in Fig. 2. We measure sweep-rate-dependent DNP profiles $P(f_r)$ with $T = 20$ s, at several regimes of optical η_e and MW η_r power. In particular, we consider four regimes of MW power between $\eta_r = 0.1$ –53 W, and for each, measure $P(f_r)$ profiles for different effective optical powers $\eta_e = 0.4$ –20.8 W. The upper and lower axes in Fig. 2 denote f_r and $f_r^{1/2}$, respectively. Solid lines are fits to Eq. (2). Optimal sweep rates f_{opt} (dashed lines) are determined from maxima of the fitted curves.

Figures 3(a) and 3(b) show obtained maximal polarizations against η_e for the MW power regimes considered (colorbar), plotted on a linear [Fig. 3(a)] and logarithmic [Fig. 3(b)] scale. Polarization here is generated at f_{opt} . Solid lines are guides to the eye. In a complementary manner, points in Fig. 3(c) display the extracted optimal rates $f_{\text{opt}}(\eta_e)$ for different MW powers. Solid lines are linear fits. Figure 3(e), in turn, plots the slope of these lines, about $df_{\text{opt}}(\eta_e)/d\eta_e$, while Fig. 3(f) plots the polarization generated using different MW powers at $\eta_e = 20.8$ W [vertical slice in Fig. 3(a)]. A combined view of Figs. 2–3 allows the ability to correlate f_{opt} to the absolute spin-injection rates achieved.

We now systematically consider factors setting f_{opt} from left to right in Fig. 2, starting from the low-MW power

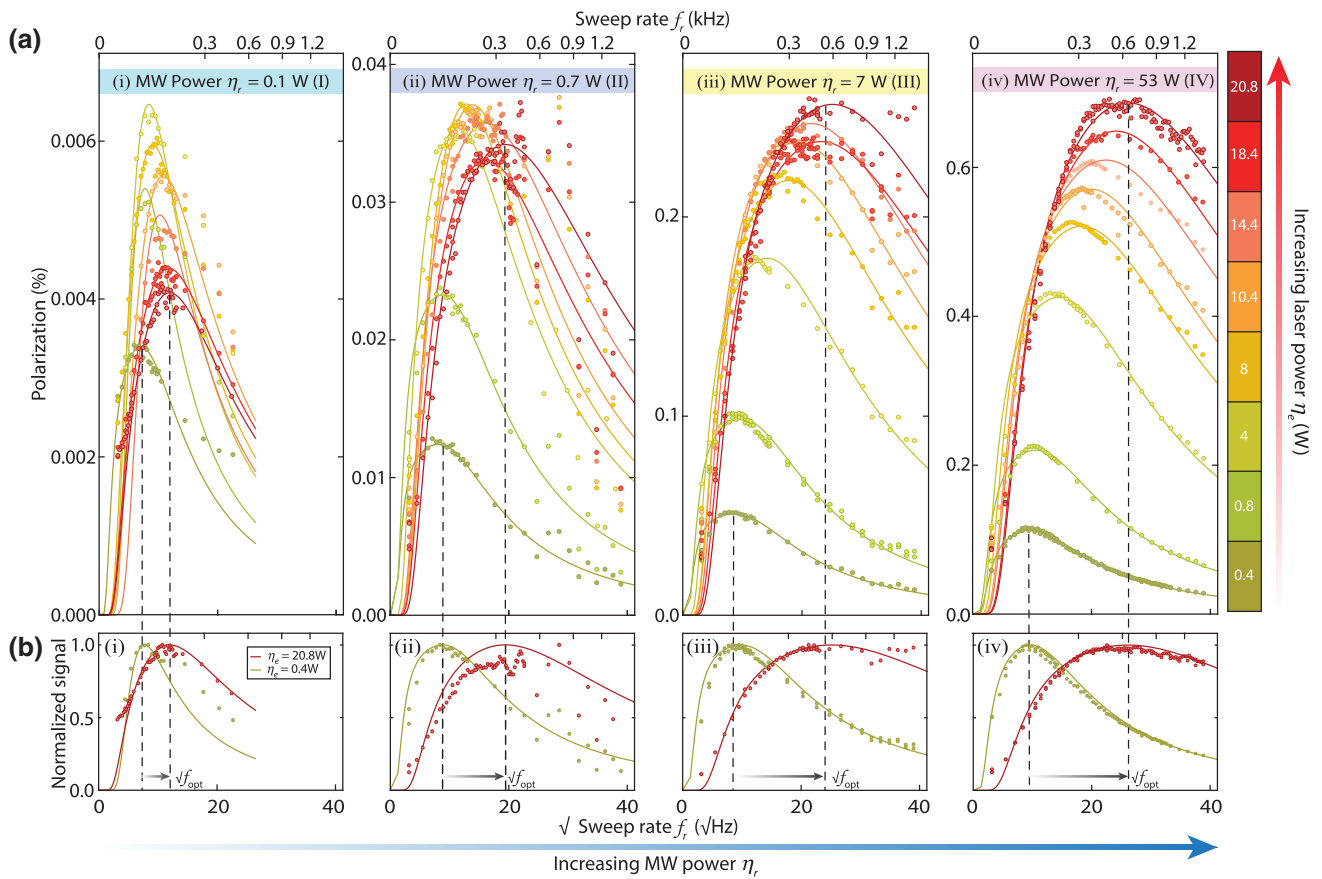


FIG. 2. Enhancing rate of polarization transfer at high laser and MW power. (a) DNP sweep rate profiles $P(f_r)$ for different regimes of MW power [(I)–(IV)] $\eta_r = 0.1$ –53 W, in each of which the laser power is varied within the range $\eta_e = 0.4$ –20.8 W (see the colorbar). Increase in f_{opt} with increasing laser power is shown (dashed lines). Polarization time $T = 20$ s. Plots are shown against $f_r^{1/2}$ (upper axes denote f_r). Solid lines are fits to the ratchet model [Eq. (2)]. Corresponding values of maximum polarization and f_{opt} are shown in Fig. 3. Here, percent polarization is calculated through comparison with a thermal signal under the same experimental conditions and using the thermal Boltzmann distribution. (b) *Normalized curves* in (a) focusing on $\eta_e = 0.4$ and 20.8 W. Dashed lines elucidate optimal rates f_{opt} [extended to (a)]. Shifts are denoted by arrows. (I)–(II) At low MW powers, clustering of curves in (a) show that f_{opt} changes slowly with η_e , yielding little polarization gain [see Figs. 3(b) and 3(c)]. (III)–(IV) At high MW powers, increasing η_e shifts f_{opt} to higher frequencies. Profiles in panels (b)(iii)–(b)(iv) are almost identical, indicating that beyond a threshold, increasing the MW power does not result in increasing f_{opt} [see Fig. 3(c)].

region (I) ($\eta_r = 0.1$ W). This regime relates to the situation in high-field DNP where the MW power is low due to technological constraints. In Fig. 2(i), we observe the DNP profiles clustered at $f_r = 50$ –120 Hz. Increasing optical power only weakly increases f_{opt} [see also Fig. 3(c)(I)], and there is little increase in hyperpolarization. This indicates a κ_r -induced speed-limit set by adiabaticity constraints—in the ratchet picture in Fig. 1(d), the energy gaps are small and sweep rates f_r required to satisfy adiabaticity are slow. Increasing optical power therefore yields no significant increase in nuclear polarization levels [see Fig. 2(a)(i)]. We observe, in fact, a slight *decrease* in polarization at high η_e [see also Fig. 3(b)], associated with the rightward shift in f_{opt} . This polarization drop is beyond the scope of Eq. (2) and challenging to model. We hypothesize that it

arises because the electrons are repolarized multiple times during each MW sweep event, including at the LZ LACs, making polarization transfer less efficient. Simultaneously, we observe oscillations in the $P(f_r)$ profiles in the high η_e - η_r regime.

Now upon increasing MW power sevenfold [Fig. 2(ii)] to regime (II) with $\eta_r = 0.7$ W, there is a larger increase in $f_{\text{opt}}(\eta_e)$ with optical power. This rightward shift in Fig. 2(b)(ii) manifests as an increased slope in Fig. 3(c)(II). Intuitively, higher η_r yields larger energy gaps in Fig. 1(d) and allows faster sweep rates. When the optical power is low, e polarization is not produced rapidly enough at the N- V source. Increasing η_e relieves this κ_e bottleneck. From Fig. 3(e), f_{opt} in regime (II) increases about twofold with respect to regime (I),

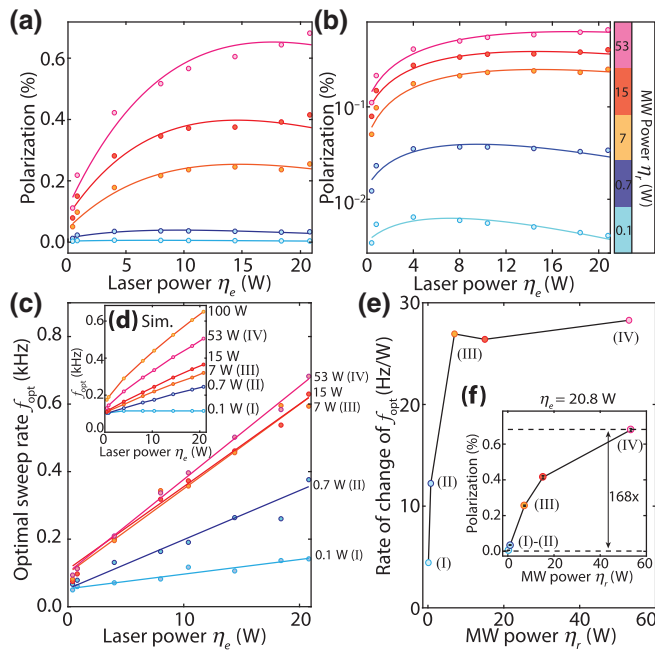


FIG. 3. Speed limits for polarization transfer. (a),(b) *Maximum polarization level* achieved in Fig. 2 plotted on a (a) linear and (b) logarithmic scale. Curves correspond to the η_r regimes studied. Combined optical-MW η_e - η_r power increase yields an approximately 200-fold boost in the hyperpolarization level. (c) *Optimal sweep rates* f_{opt} extracted from Fig. 2 for increasing η_e , at different MW power regimes [(I)–(IV)]. Points are extracted f_{opt} values, while lines are linear fits. (d) *Spin ratchet simulations* similar to (c). Slopes here continually increase with η_r due to the absence of spin diffusion. (e) *Speed up of ratchet* $df_{\text{opt}}/d\eta_e$ obtained from slopes in (c). Plateau at high MW power indicates a spin-diffusion bottleneck. (f) *Polarization increase with MW power*. Vertical slice of data in (a) at $\eta_e = 20.8$ W. Polarization begins to plateau with increasing MW power.

and there is a simultaneous increase of about 10 times in polarization [Fig. 3(b)]. However, clustering of $P(f_r)$ profiles in Fig. 2(ii), and slow growth in Fig. 3(c)(II), suggests that κ_r still limits the rate of polarization transfer.

Figure 2(iii) considers a further tenfold increase in MW power [regime (III)]. Here a rightward shift in f_{opt} is clearly evident with increasing optical power, and spin-ratchet operation is rapid, evidenced by the increased slope in Fig. 3(c)(III). Higher η_r allows faster sweeps due to weaker adiabaticity constraints, and η_e can be simultaneously boosted to increase the rate of source e polarization, yielding a *lockstep* κ_e - κ_r increase in the hyperpolarization rate. The concomitant polarization increase is evident in Figs. 3(a) and 3(b). We also note that the resulting maximal rates $f_{\text{opt}} \approx 0.65$ kHz approach, and potentially exceed, the thermal rate $T_{1e}^{-1} \sim 0.2$ kHz [44] expected in this sample.

One might expect that a further increase in MW power will continue to yield such gains. This is shown in simulations in Fig. 3(d) where we model direct $e \rightarrow n$ polarization transfer without spin diffusion. Interestingly, however,

we experimentally observe that a subsequent increase in MW power to $\eta_r = 53$ W [regime (IV)] provides no significant increase in f_{opt} [see Fig. 2(iv)]. This is also reflected in Fig. 3(c), where $f_{\text{opt}}(\eta_e)$ manifests as a series of overlapping lines beyond $\eta_r = 7$ W. This plateauing of rates is also evident in Fig. 3(e). Correspondingly, the relative polarization increases in Figs. 3(a) and 3(b) begin to slow down [see Fig. 3(f)]. Overall, this points to the presence of a third speed limit, which we ascribe to spin diffusion κ_d . Here polarization is rapidly transferred from the N- V center to proximal ^{13}C nuclei, but is limited in its ability to reach the bulk nuclei. Indeed, Figs. 3(b) and 3(c) demonstrate that, while e -polarization rates increase with η_e , nuclear spin injection is ultimately limited by spin diffusion. As such, spin injection can be considered optimally rapid in this regime.

Finally, let us quantify spin-injection gains from our strategy with respect to more conventional approaches. We attempt to make two comparisons: first, gains with respect to typical optical DNP experiments (see Appendix B), and second, gains with respect to the regime typically employed in high-field DNP. For the first case, consider spin injection with two optical powers, $\eta_e = 0.4$ and 20.8 W in regime (IV). The former is representative of powers employed previously for optical DNP [45,46] (Appendix B), and the latter corresponds to the use of the apparatus in Fig. 1(e). Figure 4(a) shows the respective polarization buildup curves. The steeper polarization growth in the latter is evident. Figure 4(b) shows the corresponding ^{13}C NMR spectra for $T = 90$ s, wherein an approximately 13-fold increase in signal is observed. Narrow spectral linewidths of approximately 16 mHz here are due to slow spin-lock decays [40]. To focus on e -proximal polarization injection separately from the strong effects of spin diffusion, Fig. 4(c) instead considers the small-time regime ($T < 0.6$ s). Polarization buildup is approximately linear in this regime; the colorbar shows the different optical powers employed. Corresponding slopes [Fig. 4(d)] permit quantification of absolute polarization injection rates (%/s) by comparing against the thermal polarization at 7 T (about 10^{-5}). Figure 4(d) demonstrates that the spin-injection rate scales approximately linearly with optical power, arising from the increased rate of source e polarization κ_e at the N- V center sites. Indeed, sustained high-power optical delivery yields an approximate 179-fold increase in polarization injection with higher-power pumping. In this case, we measure a linearized bulk injection rate of approximately 0.016%/s averaged over the sample.

For the second comparison with respect to conventional DNP, consider two MW powers, $\eta_r = 0.1$ W and $\eta_r = 53$ W [regimes (I) and (IV), respectively] at $\eta_e = 20.8$ W. The former is representative of typical MW powers in high-field DNP (without gyrotrons). From the peaks of the corresponding traces in Fig. 2, we observe an approximate

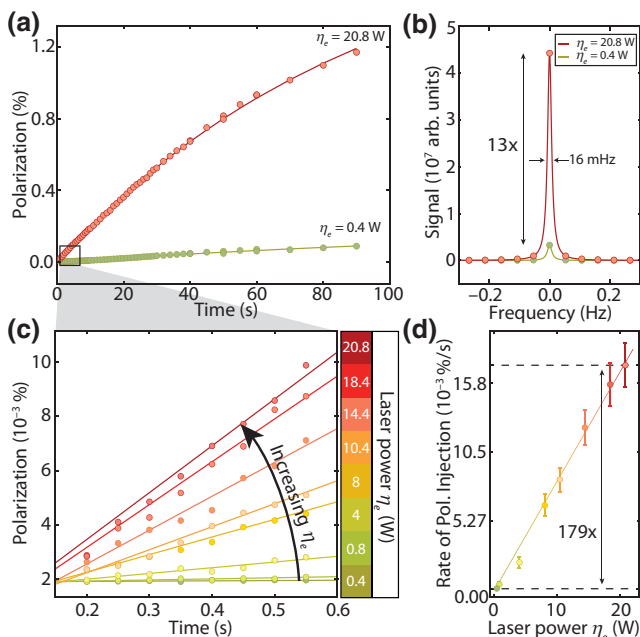


FIG. 4. Enhanced spin injection via high-power optical pumping. (a) *DNP buildup curve* in the high MW power regime (IV), $\eta_r = 53$ W with laser power $\eta_e = 0.4$ and 20.8 W. There is rapid polarization growth in the latter case. (b) *Corresponding NMR spectra* at $t = 90$ s obtained via pulsed-spin locking. Signal is enhanced approximately 13-fold for $\eta_e = 20.8$ W compared to 0.4 W optical power. DNP signal at $\eta_e = 20.8$ W corresponds to 1.17% polarization, a $> 10^3$ enhancement over the thermal signal. (c) *Short-time ^{13}C polarization growth* as a function of laser power η_e , obtained by linearizing the $T < 0.6$ s portion of the buildup curves. Colors represent different laser powers η_e (colorbar). Solid lines are linear fits. (d) *Extracted polarization injection rates* from (c) show an approximately linear increase with laser power. We obtain an approximate 179-fold boost in polarization injection when applying 20.8 W of optical power.

179-fold increase in polarization in the latter case [see Fig. 3(f)]. Overall, while a precise comparison between disparate experimental systems is difficult, data in Figs. 2 and 4 indicate that harnessing nonthermal e polarization can yield spin-injection gains by more than 2 orders of magnitude over conventional approaches.

III. DISCUSSION

Applications.—The experiments here illustrate the strength of utilizing nonthermally polarized electrons for DNP. The e polarization can be replenished at a rate $\kappa_e > T_{1e}^{-1}$, and does not require cryogenic high-field conditions. This allows access to low-field regimes where MW power can be plentiful. Simultaneously applied high optical and MW power can yield bulk spin-injection rates ultimately limited by only spin diffusion. Similar arguments can be extended to other nonthermally generated DNP approaches, including with parahydrogen [13,47,48].

The rapidly injected spin polarization here projects onto applications that exploit hyperpolarized ^{13}C spins as quantum sensors [27], leveraging their long lifetimes in the laboratory [33,49] and rotating frames [39,40]. A particularly compelling application is in nuclear spin gyroscopes; while previous work proposed [25,26,50] and demonstrated [44,51,52] gyroscopes constructed from polarized ^{14}N nuclear spins in diamond, the use of rapidly polarized ^{13}C nuclei and their relatively high spin density promises to yield significant sensitivity boosts. A similar application is the use of hyperpolarized ^{13}C nuclei as magnetometers, especially in high-field settings [27]; rapid hyperpolarization plays a critical role in enabling high sensitivity. We envision other applications in sensors for dark-matter searches [53,54], rf imaging agents [55], nuclear spin RASERS (radio-frequency amplification by stimulated emission of radiation) [30,31,56], and in condensed matter applications probing driven nonequilibrium states of matter [57].

Conclusions.—In conclusion, we demonstrate the ability to rapidly inject spin polarization into a lattice of nuclear spins, via optically polarized electrons under simultaneous high-power optical and MW irradiation. In the process, we uncover rate limits that bottleneck bulk polarization transfer in various regimes, and show that high-power excitation can yield gains in the spin-injection rate that exceed 2 orders of magnitude. Our work informs on interesting opportunities afforded by nonthermally polarized electrons for DNP and quantum sensing.

ACKNOWLEDGMENTS

We gratefully acknowledge M. Markham (Element6) for the diamond sample used in this work, and discussions with J. Reimer, C. Meriles, and D. Suter. This work is funded by the ONR under Grant No. N00014-20-1-2806. B.B. acknowledges support from a NSF Graduate Research Fellowship (DGE 2146752).

APPENDIX A: ENHANCED OPTICAL EXCITATION VIA A “LASER DOME”

Here we detail the apparatus for high-power optical illumination developed in this work. It consists of thirty lasers that deliver > 20 W of continuous, nearly isotropic, optical power to the sample. Previous experiments with N-V centers, both for DNP and quantum sensing, were predominantly in the $\eta_e < 5$ W regime (see Appendix B) and limited by sample heating [59–62]. There have been several reports of DNP with pulsed lasers [45,46]. While possessing higher peak power, they entail long dead times ($\gg T_{1e}$), where electrons are not being polarized. In contrast, the cw optical excitation here yields continuous e repolarization, and is advantageous for DNP with electrons with broad ESR spectra [35]. Furthermore, lower peak power injection here allows more efficient heat diffusion and

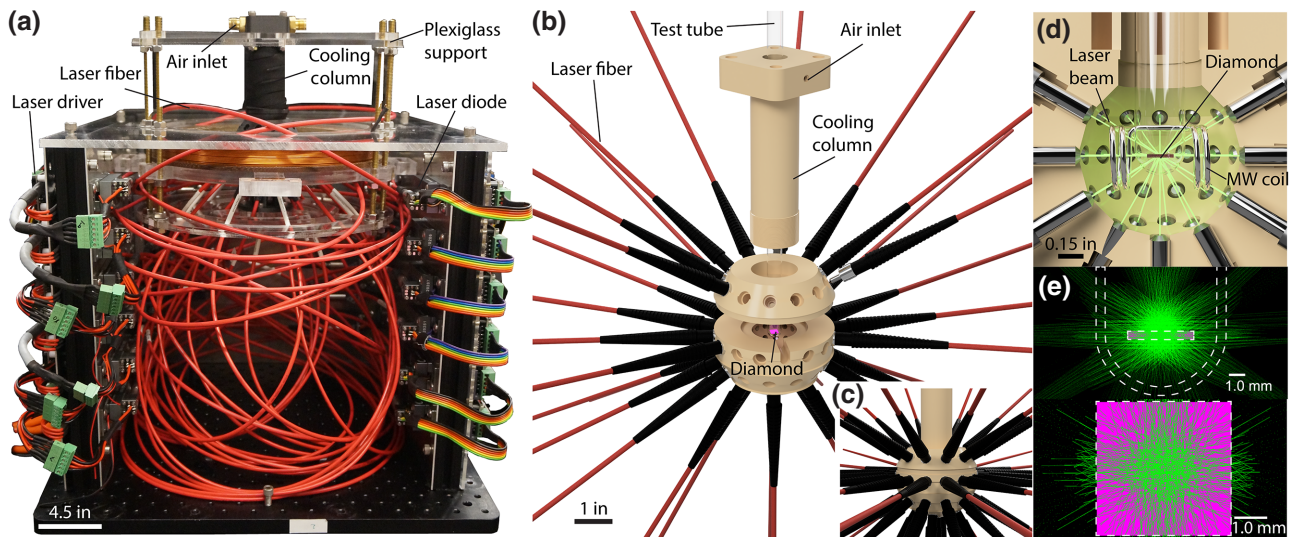


FIG. 5. Setup for high-power optical hyperpolarization. (a) *Photograph*. Thirty approximate 0.8-W lasers (mounted on vertical walls) deliver optical excitation to the sample via optical fibers. Sample is positioned at the center, with lasers arranged in a dome-shaped configuration. (b) *Laser dome* comprises a 3D printed holder for optical illumination (shown is an expanded view). Centrally aligned bores attach optical fibers via a pressure fit. Diamond is held in a test tube at the center. Neck-shaped region at the top houses a cooling column for heat exchange [see Fig. 6(a)]. (c) Rendering of the dome with lasers attached. Corresponding implementation is shown in (a). (d) *Isotropic excitation*. Enlarged image of the dome center depicting isotropic laser illumination onto the diamond sample. Split MW coil employed for hyperpolarization is shown. (e) *Geometric optics simulations* showing sample illumination from side and top views. Only refraction is modeled (attenuation is neglected).

time-averaged power before sample damage thresholds are reached.

The apparatus (shown in Fig. 5) consists of a 3D printed carbon fiber dome-shaped structure (“laser dome”) that houses the aforementioned 30 diode lasers (approximately 0.8 W each) delivered via multimode fibers (beam diameter of approximately 4 mm). More details of the construction with computer-aided design (CAD) models are presented in the Supplemental Material [63]. We exploit relaxed requirements on optical mode quality, polarization, and stability necessary for e polarization. This enables using an array of low-cost diode lasers to generate a high total optical power. The fibers are pressure fit into grooves that geometrically align towards the dome center [Fig. 5(c)]. The almost isotropic excitation pattern uniformly illuminates each of the sample facets and the exact beam arrangement is staggered for minimal overlap with the MW excitation coil [enlarged view in Fig. 5(d)]. It also allows a significantly larger sample volume to be irradiated compared to previous approaches [60,61,64], since an approximate 4π solid angle is illuminated. Ray-trace simulations depicted in Fig. 5(e) help discern the best positions of laser fibers. The density of overlapping ray traces here serves as a proxy for the relative intensity of irradiation onto the sample (see the Supplemental Material [63]). The central portion of the sample sees excitation from multiple sources that, to an extent, compensates for attenuation through it [65,66]. Although quantifying the exact penetration depth through the sample

is experimentally challenging, we estimate it to be of the order of 0.1–0.15 mm [65].

Large optical powers require the ability to mitigate sample heating. We design an *in situ* heat exchanger that efficiently ejects heat while keeping the sample free from motion. Figure 6(a) describes its operation. The sample is held in a test tube surrounded by approximately 4-mL water. Thermal energy injected into the diamond is rapidly dissipated to the water, which serves as a heat sink. The water is kept at a stable temperature by flowing cool nitrogen gas (-20°C at the inlet) across the test tube. The gas is delivered from slits built into the neck region of the laser dome [blue arrows in Fig. 6(a)]. The nitrogen flow rate is calibrated so that the water temperature is approximately 9°C when the lasers are off (see the Supplemental Material [63] for more details). Heat exchange exploits the excellent thermal conductivity of diamond ($2200\text{ Wm}^{-1}\text{ K}^{-1}$) and the large heat capacity of water for efficient thermal dissipation [red arrows in Fig. 6(a)]. The benefit of this relayed heat transfer strategy is that the cold gas does not contact the sample directly, and the sample volume can be enclosed—an advantage for shuttling to high field for detection [67].

Heat exchanger performance is found to be highly effective. Figures 6(b) and 6(c) depict the measured temperature buildup in the sample and surrounding fluid under 120 s continuous irradiation at different optical powers. After 120 s, the lasers are turned off, and the temperature dissipation is again monitored. Even at

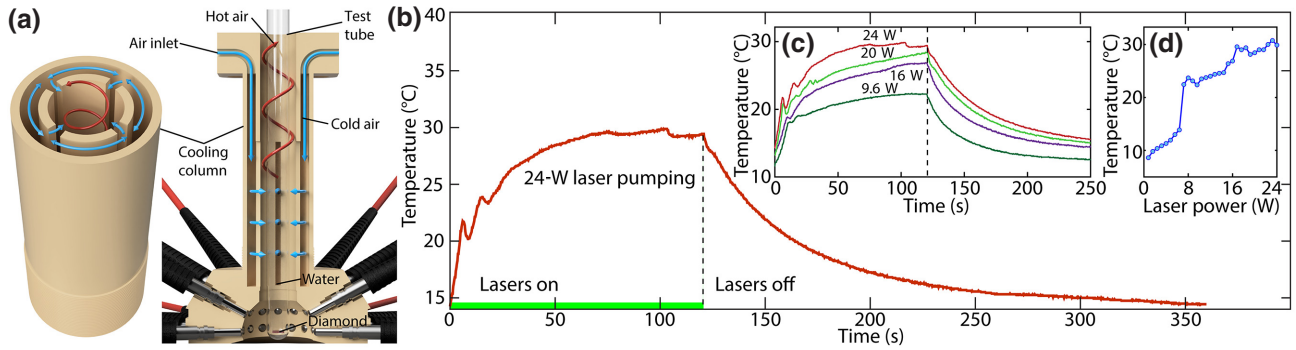


FIG. 6. Thermal management for high-power optical pumping. (a) *Sample cooling strategy*. Cross section of the laser dome neck [see Fig. 5(b)] (top and side views). N_2 gas at -20°C (blue arrows) flows through the air inlets, and actively cools the walls of the test tube carrying the water that surrounds the sample. Blue and red arrows depict cold and hot air currents, respectively. (b) *Heat exchanger performance*. Profile of heat buildup and dissipation upon 120 s of continuous 24 W optical illumination from 30 lasers and subsequent turnoff (dashed vertical line). Temperature is measured 4 mm away from the diamond sample in the test tube. Steady-state temperature does not exceed 30°C even with a sustained 2-min high-power illumination. (c) *Temperature buildup and cooling profiles* for different optical powers. Sample cooling upon laser turnoff (dashed line) occurs with an exponential time constant of approximately 1 min. (d) *Measured steady-state temperature* (after 120 s) for varying optical power applied.

sustained 24-W optical power (an intensity of approximately 0.19 kW/cm^2) employing thirty lasers, the (asymptotic) steady-state temperature is less than 30°C and no sample damage is observed. Figure 6(d) plots the steady-state temperatures for different powers. From the buildup rate, we estimate that $\gtrsim 50\text{-W}$ power can be applied before system limits (related to water boiling) are reached.

The strategy for high-power optical illumination and thermal management developed here is extensible to other systems, including organic triplet molecular systems and UV-generated nonpersistent radicals [45,68]. We envision applications to e -spin MASERS [30,31] and quantum sensors with e -spin ensembles [64,69], where reaching higher optical powers is the primary factor limiting magnetometer sensitivity [62].

APPENDIX B: COMPARISON TO PREVIOUS WORK

The table in Fig. 7 compares laser parameters of our work with other recent experimental studies focused on optically pumped DNP [17,45,46,58] and e -spin MASERS [30]. Previous literature has explored both pulsed and cw light sources at a variety of different wavelengths. We see from this table that there are several advantages to our approach. First, we employ low-cost 520-nm diode lasers that can be arrayed together to create a large continuous optical excitation power, as opposed to a singular, more expensive laser. This also exploits the very relaxed requirements on laser mode quality required for e polarization. We are able to apply significantly higher time-averaged optical power than most previous experiments. Our data [Figs. 6(b)–6(d)] indicate that scaling up to even higher power can be relatively easily accomplished. Pulsed laser systems can deliver larger peak power but are limited by

slow repetition rates. They also make the sample more susceptible to damage from intense high-power pulses [30].

APPENDIX C: DERIVATION OF THE POLARIZATION TRANSFER RATE FOR A SINGLE-SPIN RATCHET

We present here a derivation of the spin-ratchet polarization rate [Eq. (2) in the main text]. For more details on the theory, assumptions, and generalizations to large N , we refer the reader to Ref. [41]. Consider Fig. 8, where we show a single-spin ratchet ($N = 1$) with four LZ LACs in the rotating frame of the MWs, here between states of the $m_s = 0$ and $m_s = 1$ manifolds. Upon a MW sweep, there is a traversal of this cascaded LZ-LAC structure from left to right. We make the following assumptions that help simplify the theoretical evaluation of traversals, but which are reasonable under the regime of the experiments: (i) the LZ LACs are assumed to be hit sequentially so that their effects can be evaluated individually, (ii) the nuclear populations are assumed to start in the $m_s = 0$ manifold and bifurcate “down” or “right” upon encountering the LZ LACs, and (iii) N - V electronic (re)polarization is assumed to happen far away from the exact LZ-LAC points.

Consider a single traversal from left to right through the $N = 1$ LACs in Fig. 8, starting from populations restricted to the $m_s = 0$ manifold and ending with N - V repolarization. The probabilities of the possible population evolutions are then

$$\mathcal{P}(\downarrow \rightarrow \downarrow) = (1 - \mathcal{T}_1) + \mathcal{T}_1\mathcal{T}_2,$$

$$\mathcal{P}(\downarrow \rightarrow \uparrow) = \mathcal{T}_1(1 - \mathcal{T}_2),$$

$$\mathcal{P}(\uparrow \rightarrow \downarrow) = \mathcal{T}_1(1 - \mathcal{T}_2) + 2\mathcal{T}_2(1 - \mathcal{T}_2)(1 - \mathcal{T}_1),$$

$$\mathcal{P}(\uparrow \rightarrow \uparrow) = \mathcal{T}_2\mathcal{T}_1 + \mathcal{T}_2^2(1 - \mathcal{T}_1) + (1 - \mathcal{T}_2)^2(1 - \mathcal{T}_1),$$

	MASER			Dynamic nuclear polarization				
Metric	Oxborrow <i>et al.</i> (2012)	Breeze <i>et al.</i> (2018)	Eichhorn <i>et al.</i> (2012)	Tateishi <i>et al.</i> (2014)	Eichhorn <i>et al.</i> (2013)	Fischer <i>et al.</i> (2013)	King <i>et al.</i> (2015)	Present Work
System	Room-temperature pentacene	Room-temperature ¹³ C diamond	100 K naphthalene and pentacene	Room-temperature <i>p</i> -terphenyl	Ultracold pyruvate	Room-temperature ¹³ C diamond	Room-temperature ¹³ C diamond	Room-temperature ¹³ C diamond
Source	Pulsed laser	CW Laser	Pulsed laser	Pulsed laser	UV Lamp	CW Laser	CW Laser	CW Laser
Excitation	585 nm	532 nm	515 nm	594 nm	365 nm	532	532 nm	520 nm
Pulse duration	350 μs	Continuous	400 ns	1 μs	Continuous	Continuous	Continuous	Continuous
Pulse frequency	1 Hz	Continuous	400–4000 Hz	50 Hz	Continuous	Continuous	Continuous	Continuous
Irradiation time			140–2000 minutes	1–30 minutes	1 h	10 s	60 s	120 s
Pulse energy	0.5 J	Continuous	1 mJ	10 mJ	Continuous	Continuous	Continuous	Continuous
Time-averaged power	0.5 W	0.4 W	0.4–4 W	0.5 W	<0.1 W	1–5 W	1.7 W	20.8 W
Magnetic field strength	Ambient	0.43 T	0.30 T	0.40 T	5.0 T	50 mT	0.42 T	36 mT
Polarization			50%	34%	50%	0.5%	6% ^a	1.17%

FIG. 7. Table comparing our optical system (Figs. 5–6) to previous work in the literature for DNP and spin-based MASERS. Our multilaser excitation and thermal management strategy is able to deliver much higher time-averaged optical power compared to previous work. ^a We note that the polarization estimate in King *et al.* [58] did not use an internal (thermal) reference.

where $\mathcal{T}_{1,2}$ here refer to the tunneling probabilities [Fig. 8(b)], and depend on the adiabaticity of the traversal through the respective LZ LAC; for example, $\mathcal{T}_{1,2} = \exp(\varepsilon_{1,2}^2/f_r\mathcal{B})$. Indeed, each term in the expressions above can be thought of as referring to a different trajectory through the LZ-LAC structure [schematically shown in Fig. 8(b)]. For instance, there are two paths that constitute the term, $\mathcal{P}(\downarrow \rightarrow \downarrow)$, corresponding to the probabilities of $|0, \downarrow\rangle \rightarrow |0, \downarrow\rangle$ and $|0, \downarrow\rangle \rightarrow |+1, \downarrow\rangle$, respectively. Now, in order to determine the nuclear hyperpolarization, we evaluate the difference in populations between the nuclear states at the end of the sweep:

$$\begin{aligned}
 P &= [\mathcal{P}(\downarrow \rightarrow \downarrow) + \mathcal{P}(\uparrow \rightarrow \downarrow)] \\
 &\quad - [\mathcal{P}(\downarrow \rightarrow \uparrow) + \mathcal{P}(\uparrow \rightarrow \uparrow)] \\
 &= (1 - \mathcal{T}_1)[1 - (2\mathcal{T}_2 - 1)^2]. \quad (\text{C1})
 \end{aligned}$$

Ultimately, Eq. (C1) illustrates that hyperpolarization develops as a result of the differential adiabaticity of the

traversals through the pairs of LZ LACs conditioned on the nuclear state. The net hyperpolarization developed in time T has the form

$$P = \left[1 - \exp\left(\frac{-c_e\eta_e}{f_r}\right) \right] T f_r [(1 - \mathcal{T}_1)\{1 - (2\mathcal{T}_2 - 1)^2\}], \quad (\text{C2})$$

where the first term in square brackets encapsulates the starting electron polarization, $T f_r$ gives the total sweeps in time T , and the second term in square brackets is Eq. (C1). We therefore refer to the mechanism as being a “spin ratchet,” since each MW sweep event can be thought of as performing work to transfer a finite amount of polarization from the electronic spin to the directly coupled nuclei. While Eq. (2) is derived from the $N = 1$ case displayed in Fig. 8, it acts as a good approximation even at large N such as in the system in Fig. 1(a). This generalization to large N is further detailed in Ref. [41]. Here, one can show that the system comprises a cascaded structure of 2^{2N} LZ LACs,

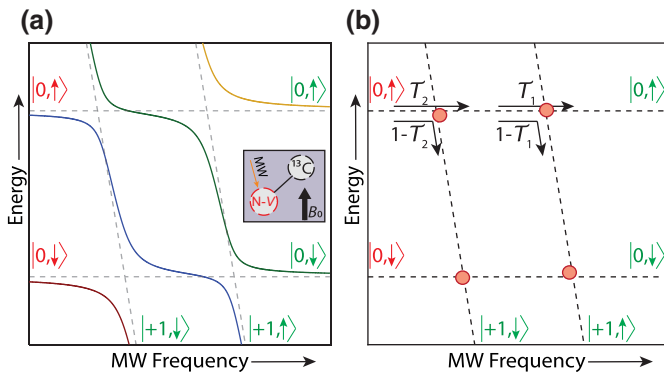


FIG. 8. Single-spin ratchet. (a) Landau-Zener level anticrossings for a system of an N-V coupled to a single ^{13}C nucleus (shown in inset) with $A^{\parallel} > 0$. Two pairs of energy gaps are visible, with the large gaps being set by the electronic Rabi frequency. The two electronic manifolds are marked. Optical pumping resets the system polarization to the $m_s = 0$ manifold, and initially the system is unpolarized, yielding equal populations in either of the $|0, \downarrow\rangle, |0, \uparrow\rangle$ states. Hyperpolarization can be excited under a MW sweep from low-to-high frequency; optimal rate of the sweep f_{opt} is determined by conditional traversals through the four LZ LACs. (b) LZ-LAC locations extracted from (a), and arranged in a checkerboard (“Galton board” [43]) of energy and frequency. Population evolution can be described using the tunneling probabilities $T_{1,2}$. Starting (red) and ending (green) nuclear states are marked.

and evolution through them can be theoretically evaluated by mapping the dynamics to the operation of a “Galton board” [41].

[1] A. Abragam and M. Goldman, Principles of dynamic nuclear polarization, *Rep. Prog. Phys.* **41**, 395 (1978).
 [2] M. Goldman, *Spin Temperature and NMR in Solids* (Clarendon Press, Oxford, 1970).
 [3] J. J. Morton, A. M. Tyryshkin, R. M. Brown, S. Shankar, B. W. Lovett, A. Ardavan, T. Schenkel, E. E. Haller, J. W. Ager, and S. Lyon, Solid-state quantum memory using the ^{31}P nuclear spin, *Nature* **455**, 1085 (2008).
 [4] H. Bluhm, S. Foletti, D. Mahalu, V. Umansky, and A. Yacoby, Enhancing the Coherence of a Spin Qubit by Operating it as a Feedback Loop That Controls Its Nuclear Spin Bath, *Phys. Rev. Lett.* **105**, 216803 (2010).
 [5] H. Bluhm, S. Foletti, I. Neder, M. Rudner, D. Mahalu, V. Umansky, and A. Yacoby, Dephasing time of gas electron-spin qubits coupled to a nuclear bath exceeding 200 μs , *Nat. Phys.* **7**, 109 (2011).
 [6] C. Kloeffel and D. Loss, Prospects for spin-based quantum computing in quantum dots, *Annu. Rev. Condens. Matter Phys.* **4**, 51 (2013).
 [7] G. D. Fuchs, G. Burkard, P. V. Klimov, and D. D. Awschalom, A quantum memory intrinsic to single nitrogen-vacancy centres in diamond, *Nat. Phys.* **7**, 789 (2011).

[8] A. Reiserer, N. Kalb, M. S. Blok, K. J. van Bemmelen, T. H. Taminiau, R. Hanson, D. J. Twitchen, and M. Markham, Robust Quantum-Network Memory Using Decoherence-Protected Subspaces of Nuclear Spins, *Phys. Rev. X* **6**, 021040 (2016).
 [9] S. Zaiser, T. Rendler, I. Jakobi, T. Wolf, S.-Y. Lee, S. Wagner, V. Bergholm, T. Schulte-Herbrüggen, P. Neumann, and J. Wrachtrup, Enhancing quantum sensing sensitivity by a quantum memory, *Nat. Commun.* **7**, 12279 (2016).
 [10] J. A. Reimer, Nuclear hyperpolarization in solids and the prospects for nuclear spintronics, *Solid State Nucl. Magn. Reson.* **37**, 3 (2010).
 [11] K. Yang, P. Willke, Y. Bae, A. Ferrón, J. L. Lado, A. Ardavan, J. Fernández-Rossier, A. J. Heinrich, and C. P. Lutz, Electrically controlled nuclear polarization of individual atoms, *Nat. Nanotechnol.* **13**, 1120 (2018).
 [12] M. Doherty, C. A. Meriles, A. Alkauskas, H. Fedder, M. J. Sellars, and N. B. Manson, Towards a Room-Temperature Spin Quantum Bus in Diamond via Electron Photoionization, Transport, and Capture, *Phys. Rev. X* **6**, 041035 (2016).
 [13] J.-B. Hövener, N. Schwaderlapp, T. Lickert, S. B. Duckett, R. E. Mewis, L. A. Highton, S. M. Kenny, G. G. Green, D. Leibfritz, J. G. Korvink, Jürgen Hennig, and Dominik von Elverfeldt, A hyperpolarized equilibrium for magnetic resonance, *Nat. Commun.* **4**, 1 (2013).
 [14] A. Henstra, P. Dirksen, J. Schmidt, and W. Wenckebach, Nuclear spin orientation via electron spin locking (novel), *J. Mag. Res.* **77**, 389 (1988).
 [15] A. Henstra, T. S. Lin, J. Schmidt, and W. T. Wenckebach, High dynamic nuclear polarization at room temperature, *Chem. Phys. Lett.* **165**, 6 (1990).
 [16] P. London, J. Scheuer, J.-M. Cai, I. Schwarz, A. Retzker, M. Plenio, M. Katagiri, T. Teraji, S. Koizumi, J. Isoya, R. Fischer, L. P. McGuinness, B. Naydenov, and F. Jelezko, Detecting and Polarizing Nuclear Spins with Double Resonance on a Single Electron Spin, *Phys. Rev. Lett.* **111**, 067601 (2013).
 [17] R. Fischer, C. O. Bretschneider, P. London, D. Budker, D. Gershoni, and L. Frydman, Bulk Nuclear Polarization Enhanced at Room Temperature by Optical Pumping, *Phys. Rev. Lett.* **111**, 057601 (2013).
 [18] A. G. Redfield, Spatial diffusion of spin energy, *Phys. Rev.* **116**, 315 (1959).
 [19] A. Abragam and M. Goldman, *Nuclear Magnetism: Order and Disorder* (Clarendon Press, Oxford, 1982).
 [20] K. R. Thurber, W.-M. Yau, and R. Tycko, Low-temperature dynamic nuclear polarization at 9.4 T with a 30 mW microwave source, *J. Magn. Reson.* **204**, 303 (2010).
 [21] A. Lund, A. Equbal, and S. Han, Tuning nuclear depolarization under MAS by electron T_{1e} , *Phys. Chem. Chem. Phys.* **20**, 23976 (2018).
 [22] L. R. Becerra, G. J. Gerfen, R. J. Temkin, D. J. Singel, and R. G. Griffin, Dynamic Nuclear Polarization with a Cyclotron Resonance Maser at 5 T, *Phys. Rev. Lett.* **71**, 3561 (1993).
 [23] T. Maly, G. T. Debelouchina, V. S. Bajaj, K.-N. Hu, C.-G. Joo, M. L. MakJurkauskas, J. R. Sirigiri, P. C. A. van der Wel, J. Herzfeld, R. J. Temkin, and R. G. Griffin, Dynamic nuclear polarization at high magnetic fields, *J. Chem. Phys.* **128**, 052211 (2008).

- [24] C. Ramanathan, Dynamic nuclear polarization and spin diffusion in nonconducting solids, *Appl. Magn. Reson.* **34**, 409 (2008).
- [25] A. Ajoy and P. Cappellaro, Stable three-axis nuclear-spin gyroscope in diamond, *Phys. Rev. A* **86**, 062104 (2012).
- [26] M. Ledbetter, K. Jensen, R. Fischer, A. Jarmola, and D. Budker, Gyroscopes based on nitrogen-vacancy centers in diamond, *Phys. Rev. A* **86**, 052116 (2012).
- [27] O. Sahin, E. d. L. Sanchez, S. Conti, A. Akkiraju, P. Reshetikhin, E. Druga, A. Aggarwal, B. Gilbert, S. Bhava, and A. Ajoy, High-field magnetometry with hyperpolarized nuclear spins, arXiv preprint [arXiv:2112.11612](https://arxiv.org/abs/2112.11612) (2021).
- [28] M. Negoro, A. Kagawa, K. Tateishi, Y. Tanaka, T. Yuasa, K. Takahashi, and M. Kitagawa, Dissolution dynamic nuclear polarization at room temperature using photoexcited triplet electrons, *J. Phys. Chem. A* **122**, 4294 (2018).
- [29] H. Kouno, K. Orihashi, K. Nishimura, Y. Kawashima, K. Tateishi, T. Uesaka, N. Kimizuka, and N. Yanai, Triplet dynamic nuclear polarization of crystalline ice using water-soluble polarizing agents, *Chem. Commun.* **56**, 3717 (2020).
- [30] M. Oxborrow, J. D. Breeze, and N. M. Alford, Room-temperature solid-state maser, *Nature* **488**, 353 (2012).
- [31] J. D. Breeze, E. Salvadori, J. Sathian, N. M. Alford, and C. W. Kay, Continuous-wave room-temperature diamond maser, *Nature* **555**, 493 (2018).
- [32] E. Reynhardt, Spin lattice relaxation of spin-1/2 nuclei in solids containing diluted paramagnetic impurity centers. I. Zeeman polarization of nuclear spin system, *Concepts Magn. Reson. Part A* **19A**, 20 (2003).
- [33] A. Ajoy, B. Safvati, R. Nazaryan, J. Oon, B. Han, P. Raghavan, R. Nirodi, A. Aguilar, K. Liu, X. Cai, X. Lv, E. Druga, C. Ramanathan, J. A. Reimer, C. A. Meriles, D. Suter, and A. Pines, Hyperpolarized relaxometry based nuclear T1 noise spectroscopy in diamond, *Nat. Commun.* **10**, 1 (2019).
- [34] A. Ajoy, K. Liu, R. Nazaryan, X. Lv, P. R. Zangara, B. Safvati, G. Wang, D. Arnold, G. Li, A. Lin, Priyanka Raghavan, Emanuel Druga, Siddharth Dhomkar, Daniela Pagliero, Jeffrey A. Reimer, Dieter Suter, Carlos A. Meriles, and Alexander Pines, Orientation-independent room temperature optical ^{13}C hyperpolarization in powdered diamond, *Sci. Adv.* **4**, eaar5492 (2018).
- [35] A. Ajoy, R. Nazaryan, K. Liu, X. Lv, B. Safvati, G. Wang, E. Druga, J. Reimer, D. Suter, C. Ramanathan, C. A. Meriles, and A. Pines, Enhanced dynamic nuclear polarization via swept microwave frequency combs, *Proc. Natl. Acad. Sci.* **115**, 10576 (2018).
- [36] B. Grotz, M. V. Hauf, M. Dankerl, B. Naydenov, S. Pezzagna, J. Meijer, F. Jelezko, J. Wrachtrup, M. Stutzmann, F. Reinhard, and Jose A. Garrido, Charge state manipulation of qubits in diamond, *Nat. Commun.* **3**, 1 (2012).
- [37] N. Aslam, G. Waldherr, P. Neumann, F. Jelezko, and J. Wrachtrup, Photo-induced ionization dynamics of the nitrogen vacancy defect in diamond investigated by single-shot charge state detection, *New J. Phys.* **15**, 013064 (2013).
- [38] W.-K. Rhim, D. Burum, and D. Elleman, Multiple-Pulse Spin Locking in Dipolar Solids, *Phys. Rev. Lett.* **37**, 1764 (1976).
- [39] A. Ajoy, R. Nirodi, A. Sarkar, P. Reshetikhin, E. Druga, A. Akkiraju, M. McAllister, G. Maineri, S. Le, and A. Lin *et al.*, Dynamical decoupling in interacting systems: Applications to signal-enhanced hyperpolarized readout, arXiv preprint [arXiv:2008.08323](https://arxiv.org/abs/2008.08323) (2020).
- [40] W. Beatrez, O. Janes, A. Akkiraju, A. Pillai, A. Oddo, P. Reshetikhin, E. Druga, M. McAllister, M. Elo, B. Gilbert, D. Suter, and A. Ajoy, Floquet Prethermalization with Lifetime Exceeding 90 s in a Bulk Hyperpolarized Solid, *Phys. Rev. Lett.* **127**, 170603 (2021).
- [41] M. Elanchezhian, A. Pillai, T. Virtanen, and A. Ajoy, “Galton board” nuclear hyperpolarization, arXiv preprint [arXiv:2110.05742](https://arxiv.org/abs/2110.05742) (2021).
- [42] P. R. Zangara, S. Dhomkar, A. Ajoy, K. Liu, R. Nazaryan, D. Pagliero, D. Suter, J. A. Reimer, A. Pines, and C. A. Meriles, Dynamics of frequency-swept nuclear spin optical pumping in powdered diamond at low magnetic fields, *Proc. Natl. Acad. Sci.* **116**, 201811994 (2019).
- [43] A. Pillai, M. Elanchezhian, T. Virtanen, S. Conti, and A. Ajoy, Electron-to-nuclear spectral mapping via “Galton board” dynamic nuclear polarization, arXiv preprint [arXiv:2110.05742](https://arxiv.org/abs/2110.05742) (2021).
- [44] A. Jarmola, S. Lourette, V. M. Acosta, A. G. Birdwell, P. Blümler, D. Budker, T. Ivanov, and V. S. Malinovsky, Demonstration of diamond nuclear spin gyroscope, *Sci. Adv.* **7**, eabl3840 (2021).
- [45] T. R. Eichhorn, Y. Takado, N. Salameh, A. Capozzi, T. Cheng, J.-N. Hyacinthe, M. Mishkovsky, C. Roussel, and A. Comment, Hyperpolarization without persistent radicals for in vivo real-time metabolic imaging, *Proc. Natl. Acad. Sci.* **110**, 18064 (2013).
- [46] K. Tateishi, M. Negoro, S. Nishida, A. Kagawa, Y. Morita, and M. Kitagawa, Room temperature hyperpolarization of nuclear spins in bulk, *Proc. Natl. Acad. Sci.* **111**, 7527 (2014).
- [47] R. W. Adams, J. A. Aguilar, K. D. Atkinson, M. J. Cowley, P. I. Elliott, S. B. Duckett, G. G. Green, I. G. Khazal, J. López-Serrano, and D. C. Williamson, Reversible interactions with para-hydrogen enhance NMR sensitivity by polarization transfer, *Science* **323**, 1708 (2009).
- [48] A. N. Pravdivtsev, A. V. Yurkovskaya, H.-M. Vieth, K. L. Ivanov, and R. Kaptein, Level anti-crossings are a key factor for understanding para-hydrogen-induced hyperpolarization in sabre experiments, *ChemPhysChem* **14**, 3327 (2013).
- [49] E. Rej, T. Gaebel, T. Boele, D. E. Waddington, and D. J. Reilly, Hyperpolarized nanodiamond with long spin-relaxation times, *Nat. Commun.* **6**, 8459 (2015).
- [50] D. Maclaurin, M. W. Doherty, L. C. L. Hollenberg, and A. M. Martin, Measurable Quantum Geometric Phase from a Rotating Single Spin, *Phys. Rev. Lett.* **108**, 240403 (2012).
- [51] J.-C. Jaskula, K. Saha, A. Ajoy, D. J. Twitchen, M. Markham, and P. Cappellaro, Cross-Sensor Feedback Stabilization of an Emulated Quantum Spin Gyroscope, *Phys. Rev. Appl.* **11**, 054010 (2019).
- [52] V. V. Soshenko, S. V. Bolshedvorskii, O. Rubinas, V. N. Sorokin, A. N. Smolyaninov, V. V. Vorobyov, and A. V. Akimov, Nuclear Spin Gyroscope based on the Nitrogen Vacancy Center in Diamond, *Phys. Rev. Lett.* **126**, 197702 (2021).
- [53] D. Aybas *et al.*, Search for Axionlike Dark Matter Using Solid-State Nuclear Magnetic Resonance, *Phys. Rev. Lett.* **126**, 141802 (2021).

- [54] A. Garcon, D. Aybas, J. W. Blanchard, G. Centers, N. L. Figueroa, P. W. Graham, D. F. J. Kimball, S. Rajendran, M. G. Sendra, and A. O. Sushkov *et al.*, The cosmic axion spin precession experiment (CASPER): A dark-matter search with nuclear magnetic resonance, *Quantum Sci. Technol.* **3**, 014008 (2017).
- [55] X. Lv, J. Walton, E. Druga, F. Wang, A. Aguilar, T. McKennelly, R. Nazaryan, L. Wu, O. Shenderova, and D. Vigneron *et al.*, High contrast dual-mode optical and ^{13}C magnetic resonance imaging in diamond particles, arXiv preprint [arXiv:1909.08064](https://arxiv.org/abs/1909.08064) (2019).
- [56] S. Appelt, A. Kentner, S. Lehmkuhl, and B. Blümich, From laser physics to the para-hydrogen pumped raser, *Prog. Nucl. Magn. Reson. Spectrosc.* **114**, 1 (2019).
- [57] W. Beatrez, C. Fleckenstein, A. Pillai, E. Sanchez, A. Akkijaraju, J. Alcalá, S. Conti, P. Reshetikhin, E. Druga, and M. Bukov *et al.*, Observation of a long-lived prethermal discrete time crystal created by two-frequency driving, arXiv preprint [arXiv:2201.02162](https://arxiv.org/abs/2201.02162) (2022).
- [58] J. P. King, K. Jeong, C. C. Vassiliou, C. S. Shin, R. H. Page, C. E. Avalos, H.-J. Wang, and A. Pines, Room-temperature in situ nuclear spin hyperpolarization from optically pumped nitrogen vacancy centres in diamond, *Nat. Commun.* **6**, 8965 (2015).
- [59] R. Wunderlich, J. Kohlrautz, B. Abel, J. Haase, and J. Meijer, Optically induced cross relaxation via nitrogen-related defects for bulk diamond ^{13}C hyperpolarization, *Phys. Rev. B* **96**, 220407 (2017).
- [60] D. Pagliero, K. K. Rao, P. R. Zangara, S. Dhomkar, H. H. Wong, A. Abril, N. Aslam, A. Parker, J. King, C. E. Avalos, Ashok Ajoy, Joerg Wrachtrup, Alexander Pines, and Carlos A. Meriles, Multispin-assisted optical pumping of bulk ^{13}C nuclear spin polarization in diamond, *Phys. Rev. B* **97**, 024422 (2018).
- [61] A. Ajoy, R. Nazaryan, E. Druga, K. Liu, A. Aguilar, B. Han, M. Gierth, J. T. Oon, B. Safvati, R. Tsang, J. H. Walton, D. Suter, C. A. Meriles, J. A. Reimer, and A. Pines, Room temperature “optical nanodiamond hyperpolarizer”: Physics, design, and operation, *Rev. Sci. Instrum.* **91**, 023106 (2020).
- [62] J. F. Barry, J. M. Schloss, E. Bauch, M. J. Turner, C. A. Hart, L. M. Pham, and R. L. Walsworth, Sensitivity optimization for NV-diamond magnetometry, *Rev. Mod. Phys.* **92**, 015004 (2020).
- [63] See Supplemental Material at <http://link.aps.org/supplemental/10.1103/PhysRevApplied.18.034079> for further details on the experimental apparatus.
- [64] T. Wolf, P. Neumann, K. Nakamura, H. Sumiya, T. Ohshima, J. Isoya, and J. Wrachtrup, Subpicotesla Diamond Magnetometry, *Phys. Rev. X* **5**, 041001 (2015).
- [65] V. M. Acosta, E. Bauch, M. P. Ledbetter, C. Santori, K.-M. C. Fu, P. E. Barclay, R. G. Beausoleil, H. Linget, J. F. Roch, F. Treussart, S. Chemerisov, W. Gawlik, and D. Budker, Diamonds with a high density of nitrogen-vacancy centers for magnetometry applications, *Phys. Rev. B* **80**, 115202 (2009).
- [66] S. Mui, K. Ramaswamy, and S. E. Hayes, Physical insights from a penetration depth model of optically pumped NMR, *J. Chem. Phys.* **128**, 052303 (2008).
- [67] A. Ajoy, X. Lv, E. Druga, K. Liu, B. Safvati, A. Morabe, M. Fenton, R. Nazaryan, S. Patel, T. F. Sjolander, J. A. Reimer, D. Sakellariou, C. A. Meriles, and A. Pines, Wide dynamic range magnetic field cyclers: Harnessing quantum control at low and high fields, *Rev. Sci. Instrum.* **90**, 013112 (2019).
- [68] A. Capozzi, T. Cheng, G. Boero, C. Roussel, and A. Comment, Thermal annihilation of photo-induced radicals following dynamic nuclear polarization to produce transportable frozen hyperpolarized ^{13}C -substrates, *Nat. Commun.* **8**, 15757 (2017).
- [69] D. Le Sage, L. M. Pham, N. Bar-Gill, C. Belthangady, M. D. Lukin, A. Yacoby, and R. L. Walsworth, Efficient photon detection from color centers in a diamond optical waveguide, *Phys. Rev. B* **85**, 121202 (2012).